NOTE

Susceptibility-Induced Distortion Correction in Hyperpolarized Echo Planar Imaging

Jack J. Miller [1,2]* Angus Z. Lau,[2,3] and Damian J. Tyler[1]

Purpose: Echo planar imaging is an attractive rapid imaging readout that can image hyperpolarized compounds in vivo. By alternating the sign of the phase encoding gradient waveform, spatial offsets arising from uncertain frequency shifts can be determined. We show here that blip-reversed echo planar imaging can also be used to correct for susceptibility and B_0 inhomogeneity effects that would otherwise produce image-domain distortion in the heart.

Methods: Previously acquired blip-reversed cardiac 3D-Spectral-Spatial echo planar imaging volumetric timecourses of hyperpolarized [1-^{13}C]pyruvate were distortion corrected by a deformation field estimated by reconstructing signal-to-noise ratio (SNR)-weighted progressively subsampled temporally summed images of each metabolite.

Results: Reconstructing blip-reversed data as proposed produced volumetric timecourses that overlaid with proton reference images more consistently than without such corrections.

Conclusion: The method proposed may form an attractive method to correct for image-domain distortions in hyperpolarized echo planar imaging experiments. **Magn Reson Med 000:000–000, 2017.**

Key words: magnetic resonance spectroscopy; hyperpolarized 13 C; echo planar imaging; distortion correction

INTRODUCTION

Hyperpolarized [1-^{13}C]pyruvate forms a versatile metabolic probe that has been used extensively to quantify cardiac metabolism and pH in health and disease (1–5). Many conditions where metabolic dysregulation is implicated are often spatially localized, such as myocardial ischaemia. It is challenging to image hyperpolarized compounds in the heart for numerous reasons, predominantly (1) cardiac motion, which cannot readily be retrospectively corrected for as the observed hyperpolarized signals are inherently a function of time; and (2) the finite, decaying, and nonrenewable magnetization "reservoir" generated by hyperpolarization methods necessitates magnetization-efficient rapid imaging techniques. These issues have lead to a variety of strategies to image metabolism following the injection of hyperpolarized [1-^{13}C]pyruvate, such as EPSI (6), IDEAL CSI (7), multiband excitation based approaches (8), and spectral-spatial excitation with a variety of rapid imaging trajectories, including echo planar imaging (EPI) (9–15). Many of these methods use EPI in part because it is one of the oldest proposed rapid imaging strategies (16–18), is fast, commonly available on commercial scanners, and produces artefacts that are analytically understood.

EPI artefacts fall broadly into two categories: artefacts arising from gradient infidelity, such as the the Nyquist $\left(\frac{N}{2}\right)$ ghost, caused by eddy currents predominantly imposing an alternating phase error between different lines of k-space (19); and image-domain distortions such as compressions, expansions, tearings, and other more complex geometrical transformations that arise from susceptibility changes and their associated B_0 effects (20). In proton EPI, where image domain signal-to-noise ratio (SNR) is high, a large number of methods have been proposed to ameliorate or eliminate these imperfections, such as the use of navigator echoes to remove the linear Nyquist ghost (21), and the direct measurement of B_0 to correct for geometric distortions through the use of reference scans (22,23).

Additionally, the comparatively small bandwidths used in EPI acquisitions mean that the acquired images are prone to linear displacements if the transmitter frequency and that of the chemical species imaged differ. By alternating the sign of the phase encoding gradient between successive EPI acquisitions, Cunningham et al. have shown that it is possible to correct for the inherent uncertainty in transmitter frequency with in vivo hyperpolarized experiments by shifting both images until they overlap with each other, either manually or through the use of information theory metrics such as mutual information (24). Recently, acquisition-based methods have been proposed to ameliorate these distortions in by acquiring dual-echo EPI data, and estimating field shifts directly at the expense of increased echo time (TE) (25). In proton spin-echo diffusion weighted imaging (DWI)-EPI images, Andersson et al. (26) have likewise analytically shown how B_0 and susceptibility effects result in geometric distortions, and provide an image domain

[1]Department of Physiology, Anatomy & Genetics, Sherrington Building, University of Oxford, Oxford, United Kingdom.

[2]Department of Physics, Clarendon Laboratory, University of Oxford, Oxford, United Kingdom.

[3]Health Sciences, Sunnybrook Research Institute, Toronto, Ontario, Canada.

Grant sponsor: St. Hugh's College, Oxford an EPSRC Doctoral Prize Fellowship and Training Centre Grant (refs), and also St. Hugh's College, Oxford (JJM); Grant number: EP/J013250/1 and EP/M508111/1; Grant sponsor: British Heart Foundation; Grant number: RG/11/9/28921, FS/10/002/28078, RE/13/1/30181, FS/14/17/30634.

*Correspondence to: Jack J. Miller, DPhil., Department of Physiology, Anatomy & Genetics, Sherrington Building, University of Oxford, Parks Road, Oxford, OX1 3PT, UK. E-mail: jack.miller@dpag.ox.ac.uk

Received 20 March 2017; revised 2 June 2017; accepted 24 June 2017

DOI 10.1002/mrm.26839

Published online 00 Month 2017 in Wiley Online Library (wileyonlinelibrary.com).

formalism through which the generalized distortion field $\mathbf{K}$ can be determined given the k-space trajectory, knowledge of B_0 and other sequence parameters such as the acquisition bandwidth.

METHODS

Theory

As described previously (23,26), it is helpful to consider the EPI experiment in a linear algebra framework. If a slice of magnetization has been excited, then it is well-known that, neglecting relaxation, the signal received $S(t)$ is

$$S(t) \propto \iint (x, y) e^{iy\left(\Delta B_0(x,y)+G_f(x,y,t)+G_p(x,y,t)\right)} \, \mathrm{d}x\mathrm{d}y,$$
$$\text{or equivalently, } \mathbf{s} = \mathbf{A}\boldsymbol{\rho} \qquad [1]$$

in a matrix form, where G_f and G_p represent the time-integrals of the frequency-encoding and phase-encoding waveforms respectively. If $\Delta B_0 = 0$ everywhere, then $\mathbf{A}$ is a 2D Fourier matrix; let us denote this special case $\mathbf{F}$. If this is not the case then one can define a mapping between the "true" EPI image $\boldsymbol{\rho}$, and $\mathbf{f}$ the acquired, distorted data, as $\mathbf{f} = \mathbf{F}^{\dagger}\mathbf{A}\boldsymbol{\rho} \stackrel{\text{def}}{=} \mathbf{K}\boldsymbol{\rho}$. If $\mathbf{K}$ could be estimated (given knowledge of the proposed k-space trajectory), then this implies that undistorted images could be estimated from the acquired data as $\hat{\boldsymbol{\rho}} = \mathbf{K}^{-1}\mathbf{f}$.

Unfortunately, as $\mathbf{K}$ ultimately can represent a many-to-one or many-to-many mapping between sets of images, its inverse does not necessarily exist, and its Moore–Penrose pseudo inverse is not guaranteed to be numerically constructible: image information may be obscured by artefacts. However, as quantitatively shown in detail elsewhere (26), by acquiring blip-reversed pairs of EPI images it is possible to acquire datasets with two distinct deformation fields, $\mathbf{K}^+$ and $\mathbf{K}^-$, and obtain a preconditioned numerical problem that is computationally tractable. If knowledge of B_0 is not otherwise present, it can be shown that the deformation field $\mathbf{b} \in \mathbb{R}^3$ that is consistent with the observed data is that for which

$$\underset{\mathbf{b}}{\operatorname{argmin}} \left(\sum_{c=1}^{m} \begin{bmatrix} \mathbf{f}_{c+}^{\top} & \mathbf{f}_{c-}^{\top} \end{bmatrix} \mathbf{R}_c(\mathbf{b}) \begin{bmatrix} \mathbf{f}_{c+} \\ \mathbf{f}_{c-} \end{bmatrix} \right) \qquad [2]$$

where the sum runs over all phase encoding columns c and $\mathbf{R}$ is a distortion operator defined in terms of $\mathbf{K}^{\pm}(\mathbf{b})$. This problem is usually directly solved in a least-squares sense with parameters and starting values optimized for human neuroimaging by the program "topup" in the FMRIB software library (FSL) suite (27).

In the context of imaging hyperpolarized [1-^{13}C]pyruvate metabolism, it is not immediately clear how to construct $\mathbf{K}^{\pm}$ given that the hyperpolarized EPI experiment obtains a stack of 3D images of $1 \ldots M$ different metabolites acquired at time points $1 \ldots T$. Each image $\mathbf{f}_i$ therefore varies in both intensity and SNR over time. We expect that B_0 shifts between different metabolites are common between them, whereas gross translations will occur along the readout axis arising from the uncertainty in transmitter/receiver frequency set prior to the start of the hyperpolarized experiment relative to that of the metabolite in question.

As a consequence, it is necessary to create a pair of $\mathbf{f}^{\pm}$ images containing a region of sufficient information to provide a compact support for the algorithm defined by Equation [2] to adequately function. This is tantamount to ensuring that the condition number of $\mathbf{R}$ is reasonable, and that information encompassing all metabolites is acquired. The returned deformation fields can then be applied to all metabolites, producing two sets of undistorted images for each metabolite. Any residual alternating spatial shifts between the two unwarped images can be corrected at this point by an affine coregistration step, producing two mappings, $\mathbf{a}$ which maps $\boldsymbol{\rho}^+$ onto $\boldsymbol{\rho}^-$, say, and $\mathbf{b}$, which maps $\boldsymbol{\rho}^-$ onto $\boldsymbol{\rho}^+$. In the absence of experimental noise and numerical errors, $\mathbf{a} = \mathbf{b}^{-1}$. We require a mapping to the same frame as the proton reference, and in the presence of noise we propose the geometric mean construct $\sqrt{\sqrt{\mathbf{b}}\sqrt{\mathbf{a}}}$ to as an interpolator to the proton image space, where $\sqrt{\mathbf{a}}$ denotes the matrix square root of $\mathbf{a}$ whose eigenvalues lie in the upper half plane.

We present the following algorithm to perform these tasks:

1. Reconstruct EPI data acquired, correcting for the Nyquist ghost and performing a multicoil recombination if appropriate.
2. For each metabolite, correct for bulk frequency shifts by grossly aligning the blip-up and blip-down images along the readout direction, either manually or through iteration via an information-theory metric, such as mutual information or image self-similarity. Partial voxel shifts are implemented by applying a phase ramp in the Fourier domain.
3. Construct a pair of blip-up/blip-down SNR-weighted mean images $\mathbf{f}_{\pm}$ from all metabolites acquired, scaled to maximum metabolite level. We performed this via obtaining a mean of the SNR-weighted sum of each metabolite time course, i.e., if σ_{tm} represents the relative noise (relative to maximum signal) term in image $X^{\pm}_{xyztm}$ where t represents time, m metabolite, and the $\pm$ label denotes the overall sign of the phase encoding gradient waveform, compute
$$\mathbf{f}^{\pm} = \frac{1}{M\sum_{tm}(1/\sigma^2_{tm})} \sum_{m=1}^{M} \sum_{t=1}^{T} \frac{1}{\sigma^2_{tm}} X^{\pm}_{xyztm}. \qquad [3]$$
4. Obtain $\mathbf{b}^{\mp}$ by applying topup to $\mathbf{f}^{\pm}$, here with three levels of progressive subsampling (by factors of 4, 2, and 1) with corresponding Gaussian blurring (FWHM 8, 4, 0 pixels, respectively). A large regularization parameter was found to be required to ensure that the deformation field is smooth and slowly varying, and not unduly informed by noise and the typical disconnected field of view (FOV) that hyperpolarized datasets have compared to the brain ($\lambda = 50, 20, 2$).
5. Apply the computed $\mathbf{b}^{\mp}$ to each acquired image X to estimate a stack of undistorted images.
6. Correct for residual frequency shifts (i.e., alternating translations) via the affine registration algorithm

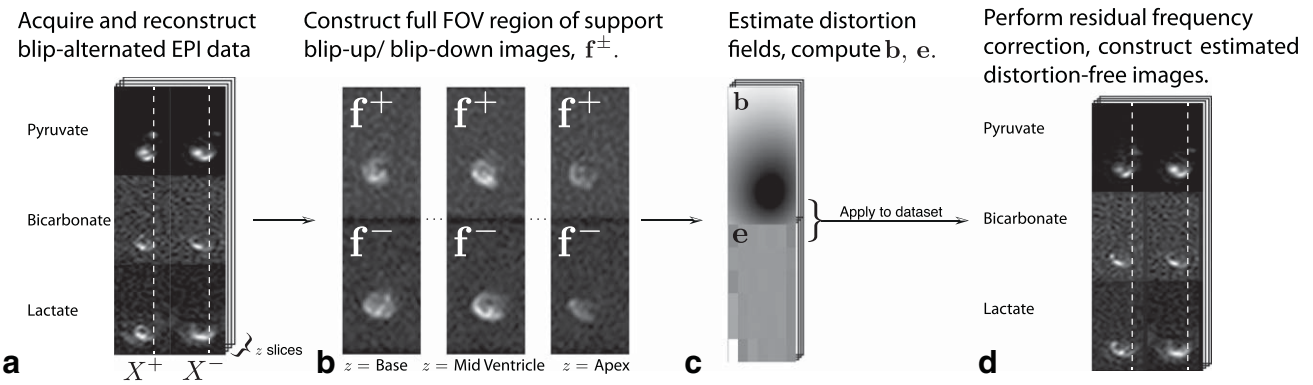

FIG. 1. An overview of the proposed distortion correction algorithm, together with illustrative example images at each stage of the process. **a**: Hyperpolarized data was acquired with alternated phase encoding blip sign; shown here are representative single mid-ventricular slice data from two adjacent time points with two different blip signs. The white dotted line illustrates nonuniform compressions and expansions arising from susceptibility effects near the heart. **b**: From these data, approximately equal-SNR $\mathbf{f}^{\pm}$ images are constructed over the whole imaging volume for distortion correction analysis. **c**: From $\mathbf{f}^{\pm}$, compute $\mathbf{b}^{\mp}$ and **e**. **d**: Hence construct estimated undistorted stacks of metabolic images, shown here at the same time points as in **1**.

separately for each metabolite, and obtain two (Hermitian) matrices $\mathbf{c}, \mathbf{d}$ mapping between the sets of images.

7. Construct the interpolator $\mathbf{e} = \sqrt{\sqrt{\mathbf{c}}\sqrt{\mathbf{d}}}$ (here via a Schur method (28,29)), apply it, and hence obtain a distortion-corrected registered volumetric stack for each time point and metabolite. Note that the Hermiticity of $\mathbf{c}$, $\mathbf{d}$ ensure that their square root exists.

The above algorithm was implemented in MATLAB and does not present a significant computational workload, requiring a few seconds to operate on $64 \times 64 \times 32 \times 20 \times 3$ matrix sizes on a Core i7–3370k workstation computer (running Linux 4.4.49-generic) with 16 GiB RAM and an NVidia Titan X GPU. Its source code (together with the experimental datasets described subsequently) can be freely downloaded from http://github.com/NeutralKaon/HPTopup.

Experimental Methods

As described previously (12), data were acquired using a 3D spectral-spatial EPI sequence with flyback excitation and a centric-ordered k-space trajectory that imaged [1-^{13}C]pyruvate, ^{13}C-bicarbonate, and [1-^{13}C]lactate in the myocardium following the intravenous infusion of [1-^{13}C]pyruvate into three anaesthetized healthy rats. Approximately 2 mL of prepolarized pyruvate was manually infused over 20 s via a tail vein cannula. The acquisition matrix size was $32 \times 16 \times 12$, FOV $64 \times 32 \times 48$ mm^3, TE= 16.34 ms, sequence length = 31.48 ms, with the flip angle $\theta = 3^\circ$ for pyruvate, or $\theta = 20^\circ$ otherwise. As each shot was prospectively gated, the repetition time (TR) was 1 RR interval, $\approx$ 150 ms. The order of acquisition was [..., Pyr^+, Bic^+, Lac^+, Pyr^-, Bic^-, Lac^-, ...] where $^{\pm}$ denotes the sign of the phase encoding gradient waveform. A two channel volume transmit/surface receive coil was used, with multicoil data recombined by the method of McKenzie (30) (which phases each image to be almost entirely real) and additionally zero-filled.

All animal experiments were performed according to relevant UK legislation. The data presented are reanalyzed versions of that acquired in the course of other ongoing studies, for which an explicit local ethical review procedure and independent cost/benefit analysis had been undertaken.

To investigate the improved spatial coregistration of the acquired hyperpolarized data with the technique, a simple phantom experiment was performed in which hyperpolarized pyruvate was injected into a syringe, and imaged as above. No shimming was performed in an attempt to mimic the variable B_0 environment of the in vivo situation. As has been previously proposed to quantify EPI distortions (31), the Jaccard self-similarity index was computed to compare the spatial distribution of acquired proton and carbon images pre- and post-correction. The Jaccard index represents the area of intersection over the area of union of two binary sets X_i and X_j, and is defined as

$$J_{ij} = \frac{|X_i \cap X_j|}{|X_i \cup X_j|}, \quad J_{ij} \in [0, 1]. \qquad [4]$$

For the phantom data, a gradient echo proton reference image was obtained, and thresholded to provide a binary mask for comparison that indicated the location of the syringe body together with a urea phantom. The temporally summed hyperpolarized image was then thresholded, and the Jaccard index for this resulting mask compared with the proton "ground truth" pre- and post-correction. Additionally, the odd- and even-echo hyperpolarized images were temporally summed, thresholded, and compared with each other: assuming that the number of frames acquired is large compared with the dynamic process of injection, these two datasets should nominally be identical were it not for distortion.

Owing to the lack of an appropriate "ground truth" image for the acquired in vivo dataset, odd- and even-echo data were temporally summed, thresholded, and the Jaccard index computed for these two sets, for each metabolite. In comparison to the phantom case, this process tacitly assumes that the frame-rate (of 1.2 s/3D image) is high compared to any biological process that could conceivably lead to a difference between odd- and even-echo images.

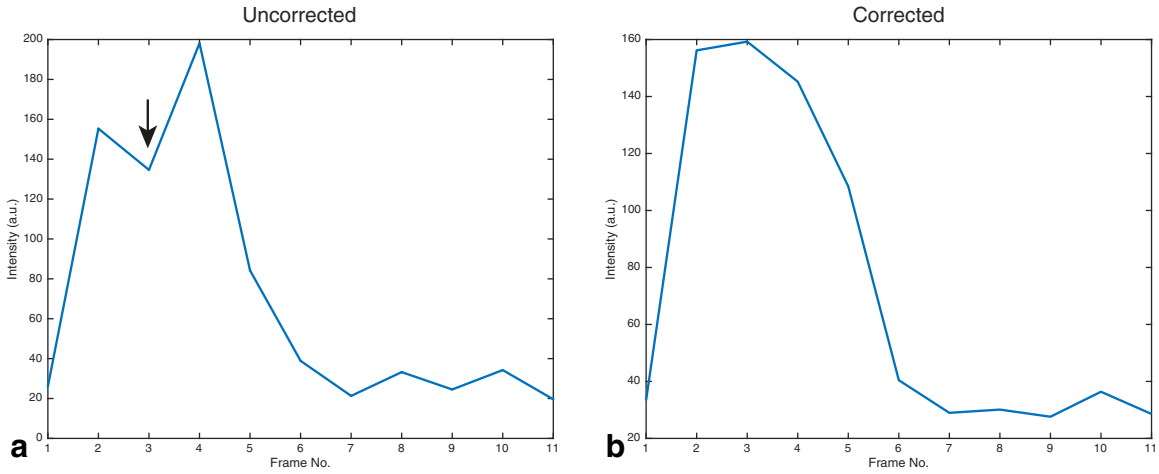

FIG. 2. Intensity of a single voxel along the edge of the ventricular line drawn in Figure 1 through time, prior to (**a**) and after (**b**) the distortion correction algorithm. The increase in amplitude of the first marked frame (and the decrease in amplitude of the point immediately adjacent to it) is consistent with the removal of an expansion/compression artefact respectively, which would be expected to alternate between frames of the acquisition.

RESULTS

We found that the method proposed is able to correct for susceptibility artefacts arising in the rodent heart, even in the low SNR environment of hyperpolarized imaging experiments. A graphical summary of the method is shown in Figure 1, illustrating the nonlinear compression and expansion artefacts that can be present in EPI readouts (Fig. 1a), the subsequent calculation of the images $\mathbf{f}^{\pm}$ (Fig. 1b), and distortion field **b** (Fig. 1c). This enables the subsequent amelioration of such artefacts (Fig. 1d).

By plotting the through-time behavior of a single voxel any compression/stretching artefacts present would be observed as alternating regions of high/low signal on alternate frames, as the object imaged "moves" between acquisitions. Figure 2 shows such a profile for a pyruvate voxel within the line profile shown in Figure 1, at the edge of the heart where susceptibility artefacts are expected to be greatest, both prior to and after the use of the proposed algorithm. Three example datasets processed with and without the proposed method are shown concatenated through space as Supporting Videos S1–S6. It is apparent that the alternating compression/extension artefact is ameliorated in these three distinct experiments.

As illustrated in Figure 3, it was found that images reconstructed through the proposed technique had less apparent variation when overlaid onto simultaneously acquired proton references. Specifically, the oscillating compression/expansion distortions caused during the EPI readout combined with small frequency errors on the order of 20 Hz results in an apparent blurring in images when temporally summed, and hence potentially misleading discrepancies between metabolite location and anatomy. Ameliorating these distortions therefore reduced the apparent width in the reconstructed image domain, and additionally increased apparent SNR in the temporally summed images due to the "constructive" addition within voxels. Supporting Videos S7–S8 contain the contents of Figure 3 without the temporal summation, and illustrates the acquired distorted data (Supporting Video S7) and that after correction (Supporting Video S8).

For the case of the phantom scanned, it was found that the Jaccard index between the thresholded proton and carbon images was increased from 0.26 to 0.29 by the distortion correction method, with masks that are illustrated in Figure 4a. The effect of the differing coil sensitivity profiles

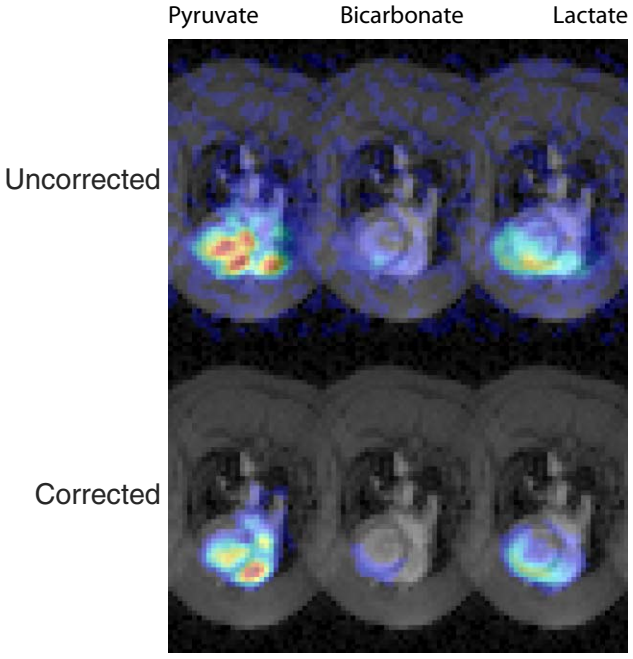

FIG. 3. Basal single-slice images of pyruvate, bicarbonate, and lactate summed over time and shown overlaid on a corresponding proton image. The color axis scale is common to both images, with transparent set to 0.2× the maximum signal obtained. As a consequence, the oscillating susceptibility errors are apparent in the summed image as a discrepancy between the observed anatomy and the expected signal location. The proposed method appears to ameliorate this, and shows pyruvate perfusion in the ventricles and metabolite production solely within the myocardium.

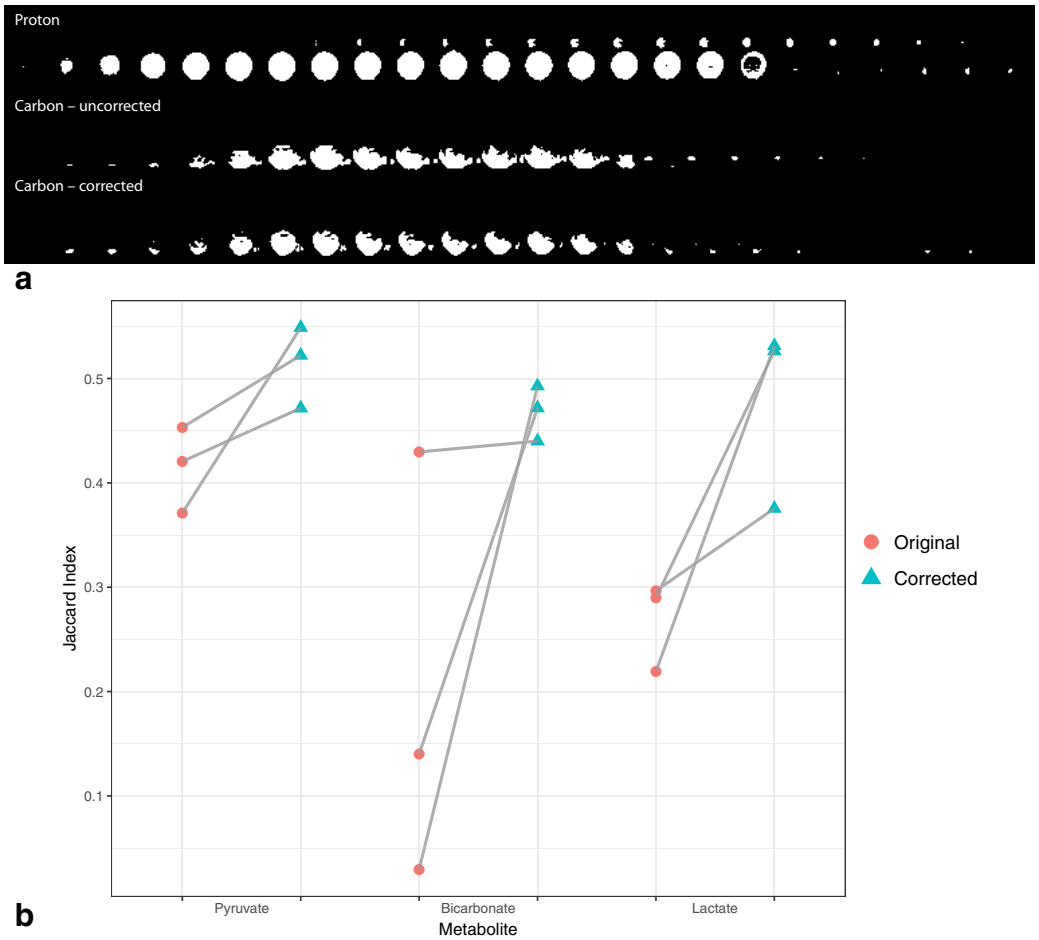

FIG. 4. **a**: Proton (top), pre-correction (middle), and post-correction (bottom) thresholded masks obtained from the distortion correction process. While thresholding ameliorates the effects of the coil sensitivity profile to some degree, it is apparent that the reduced spatial extent of B_1^- in the carbon surface array used is still visible. **b**: The Jaccard index comparing temporally summed odd and even echoes before and after correction in vivo shows a significant increase in the similarity of the image masks ($P < 0.05$), reflecting reduced distortions.

in this comparison could not be easily corrected for. In contrast, the Jaccard index computed between temporally summed odd and even echoes—which should nominally be identical given the long T_1 of pyruvate in water—increased from 0.29 to 0.76, reflecting the greatly ameliorated oscillating distortions in the images. We believe that this difference arises due to the smaller spatial extent of B_1^- provided by the carbon surface receive array used.

In vivo, we found that the Jaccard index computed as described above was increased in every metabolite and every animal scanned, as shown in Figure 4b. The median score was significantly increased in every group when considered via a nonparametric ANOVA method (the Kruskal–Wallis rank sum test (32,33)), and the mean effect of correction was significant via one-way ANOVA (which perhaps erroneously assumes normality; $P < 0.05$ in both cases). We believe that the effect of the method to increase overlap between odd- and even-echoes effectively is indicative of its utility in correcting distortions, as no differences in signal intensity between summed odd and even echoes could be visually observed in the data. All data presented are provided as examples in the source code repository for the method, and all statistical comparisons were performed in R (34).

DISCUSSION AND CONCLUSION

We have shown that existing image-domain distortion correction algorithms can be applied with slight modification to hyperpolarized EPI datasets that necessarily do not have consistently high SNR within a small, singly-connected region of the acquired image. The method we have proposed requires no additional reference scan, and has a spatial region of support that is determined entirely from the acquired data. As hyperpolarized compounds may be present with evolving shifts in regions that are spatially distinct from structures that could conceivably be localized via proton references the use of reference-free methods is attractive. For example, while hyperpolarized pyruvate has been used to characterize the inflammatory response of the lung to injury (35–37), it is likely to not be possible to obtain reference proton B_0 maps of the lung parenchyma with the same spatial extent as the acquired hyperpolarized data owing to the low tissue density within the lung.

In regions far away from the heart, such as the liver and abdominal aorta, the method was able to correct for oscillating spatial shifts that could not be corrected for via bulk frequency adjustments (cf. inferior slices in Supporting Videos S1–2 and S5–6). As it is not possible to ensure B_0

homogeneity across the entire volume of a subject, it is usually the case that the shimming process optimizes B_0 homogeneity over a region of interest, chosen here to be the heart. Typically the B_0 homogeneity in regions outside the region of interest therefore decreases as a consequence of the design of spherical harmonic shimsets. The use of image-domain distortion correction algorithms therefore allows for the amelioration of artefacts in regions that may be of secondary interest when compared to the primary region of interest that was initially proscribed for the experiment, although we stress that the method assumes that inherent chemical shift differences are already accounted for prior to its invocation. Similarly, as it is not readily possible to rapidly repeat hyperpolarized experiments should an error be discovered, such techniques therefore minimize the cost of a slight error in FOV planning.

Like all image domain methods, that proposed here relies upon sufficient SNR in the acquired data. In this work, the use of regularization and progressive subsampling limits the potentially deleterious effects of noise by effectively initially low-pass filtering the acquired data to ensure that smoothly varying B_0 fluctuations are corrected for first, and that the returned deformation mesh is smoothly varying. In the limit as SNR tends to zero, it is therefore expected to be relatively robust, and return $\mathbf{b}$ that correspond to a generalized identity matrix. This property is advantageous in hyperpolarized experiments, where the period of acquisition is usually chosen to contain a set of zero SNR images either side of the bolus of injected contrast agent.

It is difficult to directly compare distortion correction methods for hyperpolarized datasets, as there is no underlying "ground truth" image with which they can be compared. Likewise, information theory metrics such as image self-similarity or mutual information that measure generalized similarity between images by statistical means do not provide a useful metric for comparison between multidimensional images with drastically different intensity profiles, such as that examined here. The quantitative comparison undertaken here is simplistic, and relies upon thresholding the images into "signal" and "noise," a process that is potentially subjective and inherently neglects intensity variation. Consequently, a quantitative framework to assess hyperpolarized distortion correction methods represents an area for future work.

The use of image-domain distortion correction algorithms, such as that proposed here, can ameliorate susceptibility artefacts present in all EPI readouts, including those of hyperpolarized experiments. The nonuniform and temporally varying SNR necessarily present within hyperpolarized experiments necessitates care in their application to the data. We have shown a particular algorithm is able to ameliorate image-domain shifts and better coregister acquired data to underlying anatomy.

ACKNOWLEDGMENTS

We would like to acknowledge the National Institute for Health Research Oxford Biomedical Research Centre program. JJM would like to thank Nvidia Corporation for the gift of a GPU which was used in this work, and Jesper Anderson for both maintaining topup and promptly fixing segfaults that the author identified in the course of this work.

REFERENCES

1. Le Page LM, Ball DR, Ball V, Dodd MS, Miller JJ, Heather LC, Tyler DJ. Simultaneous in vivo assessment of cardiac and hepatic metabolism in the diabetic rat using hyperpolarized MRS. NMR Biomed 2016;29:1759–1767.
2. Lewis AJM, Miller JJJ, McCallum C, Rider OJ, Neubauer S, Heather LC, Tyler DJ. Assessment of metformin-induced changes in cardiac and hepatic redox state using hyperpolarized[1–13C]pyruvate. Diabetes 2016;65:3544–3551.
3. Lau AZ, Miller JJ, Tyler DJ. Mapping of intracellular pH in the in vivo rodent heart using hyperpolarized [1–13C]pyruvate. Magn Reson Med 2017;77:1810–1817.
4. Seymour AML, Giles L, Ball V, Miller JJ, Clarke K, Carr CA, Tyler DJ. In vivo assessment of cardiac metabolism and function in the abdominal aortic banding model of compensated cardiac hypertrophy. Cardiovasc Res 2015;106:249–260.
5. Schroeder MA, Cochlin LE, Heather LC, Clarke K, Radda GK, Tyler DJ. In vivo assessment of pyruvate dehydrogenase flux in the heart using hyperpolarized carbon-13 magnetic resonance. Proc Natl Acad Sci USA 2008;105:12051–12056.
6. Yen YF, Kohler SJ, Chen AP, et al. Imaging considerations for in vivo 13C metabolic mapping using hyperpolarized 13C-pyruvate. Magn Reson Med 2009;62:1–10.
7. Wiesinger F, Weidl E, Menzel MI, Janich MA, Khegai O, Glaser SJ, Haase A, Schwaiger M, Schulte RF. IDEAL spiral CSI for dynamic metabolic MR imaging of hyperpolarized [1–13C]pyruvate. Magn Reson Med 2012;68:8–16.
8. Von Morze C, Reed G, Shin P, Larson PEZ, Hu S, Bok R, Vigneron DB. Multi-band frequency encoding method for metabolic imaging with hyperpolarized [1- 13C]pyruvate. J Magn Reson 2011;211:109–113.
9. Cunningham CH, Chen AP, Lustig M, et al. Pulse sequence for dynamic volumetric imaging of hyperpolarized metabolic products. J Magn Reson 2008;193:139–146.
10. Scholz DJ, Janich MA, Köllisch U, Schulte RF, Ardenkjaer-Larsen JH, Frank A, Haase A, Schwaiger M, Menzel MI. Quantified pH imaging with hyperpolarized 13C-bicarbonate. Magn Reson Med 2015;73:2274–2282.
11. Schulte RF, Sperl JI, Weidl E, et al. Saturation-recovery metabolic-exchange rate imaging with hyperpolarized [1-(13) C] pyruvate using spectral-spatial excitation. Magn Reson Med 2012;69:1209–1216.
12. Miller JJ, Lau AZ, Teh I, Schneider JE, Kinchesh P, Smart S, Ball V, Sibson NR, Tyler DJ. Robust and high resolution hyperpolarized metabolic imaging of the rat heart at 7T with 3D spectral-spatial EPI. Magn Reson Med 2015;75:1515–1524.
13. Lau AZ, Chen AP, Hurd RE, Cunningham CH. Spectral-spatial excitation for rapid imaging of DNP compounds. NMR Biomed 2011;24:988–996.
14. Geraghty BJ, Lau JYC, Chen AP, Cunningham CH. Accelerated 3D echo-planar imaging with compressed sensing for time-resolved hyperpolarized 13C studies. Magn Reson Med 2017;77:538–546.
15. Lau AZ, Chen AP, Ghugre NR, Ramanan V, Lam WW, Connelly KA, Wright GA, Cunningham CH. Rapid multislice imaging of hyperpolarized 13C pyruvate and bicarbonate in the heart. Magn Reson Med 2010;64:1323–1331.
16. Mansfield P. Multi-planar image formation using NMR spin echoes. J Phys C Solid State Phys 1977;10:L55–L58.
17. Ahn CB, Kim JH, Cho ZH. High-speed spiral-scan echo planar NMR imaging. IEEE Trans Med Imaging 1986;5:2–7.
18. Stehling M, Turner R, Mansfield P. Echo-planar imaging: magnetic resonance imaging in a fraction of a second. Science 1991;254:43–50.
19. Bernstein MA, King KF, Zhou XJ. Handbook of MRI pulse sequences. Oxford, United Kingdom: Elsevier; 2004.
20. Munger P, Crelier GR, Peters TM, Pike GB. An inverse problem approach to the correction of distortion in EPI images. IEEE Trans Med Imaging 2000;19:681–689.
21. Bruder H, Fischer H, Reinfelder H, Schmitt F. Image reconstruction for echo planar imaging with nonequidistant kspace sampling. Magn Reson Med 1992;23:311–323.

22. Jezzard P, Balaban RS. Correction for geometric distortion in echo-planar images from B0 field variations. Magn Reson Med 1995;34:65–73.
23. Jenkinson M. Improved unwarping of EPI images using regularised B0 maps. Neuroimage 2001;13:165.
24. Cunningham CH, Dominguez Viqueira W, Hurd RE, Chen AP. Frequency correction method for improved spatial correlation of hyperpolarized 13C metabolites and anatomy. NMR Biomed 2014;27:212–218.
25. Geraghty BJ, Lau JYC, Chen AP, Cunningham CH. Dual-Echo EPI sequence for integrated distortion correction in 3D time-resolved hyperpolarized 13C MRI. Magn Reson Med 2017. doi:10.1002/mrm.26698
26. Andersson JLR, Skare S, Ashburner J. How to correct susceptibility distortions in spin-echo echo-planar images: application to diffusion tensor imaging. Neuroimage 2003;20:870–888.
27. Jenkinson M, Beckmann CF, Behrens TEJ, Woolrich MW, Smith SM. FSL. Neuroimage 2012;62:782–790.
28. Björck Å, Hammarling S. A Schur method for the square root of a matrix. Report no. C. Linear Algebra Appl 1983;52–53:127–140.
29. Higham NJ. A new sqrtm for Matlab, 1999.
30. McKenzie CA, Yeh EN, Ohliger MA, Price MD, Sodickson DK. Self-calibrating parallel imaging with automatic coil sensitivity extraction. Magn Reson Med 2002;47:529–538.
31. Tovar DA, Zhan W, Rajan SS, Auerbach E, Ramanna S, Glasser M. A rotational cylindrical fMRI phantom for image quality control. PLoS One 2015;10:e0143172.
32. Kruskal WH. A nonparametric test for the several sample problem. Ann Math Stat 1952;23:525–540.
33. Feir-Walsh BJ, Toothaker LE. An empirical comparison of the ANOVA F-test, normal scores test and Kruskal-Wallis test under violation of assumptions. Educ Psychol Meas 1974;34:789–799.
34. R Core Team. R: A language and environment for statistical computing. R Foundation for Statistical Computing. Vienna, Austria; 2014. http://www.blopig.com/blog/2013/07/citing-r-packages-in-your-thesispaperassignments/
35. Drachman N, Kadlecek S, Pourfathi M, Xin Y, Profka H, Rizi R. In vivo pH mapping of injured lungs using hyperpolarized [1–13C]pyruvate 2016. doi:10.1002/mrm.26473
36. Shaghaghi H, Kadlecek S, Deshpande C, Siddiqui S, Martinez D, Pourfathi M, Hamedani H, Ishii M, Profka H, Rizi R. Metabolic spectroscopy of inflammation in a bleomycin-induced lung injury model using hyperpolarized 1-13C pyruvate. NMR Biomed 2014;27:939–947.
37. Thind K, Chen A, Friesen-Waldner L, Ouriadov A, Scholl TJ, FoxM, Wong E, VanDyk J, Hope A, Santyr G. Detection of radiation-induced lung injury using hyperpolarized 13C magnetic resonance spectroscopy and imaging. Magn Reson Med 2013;70:601–609.

SUPPORTING INFORMATION

Additional Supporting Information may be found in the online version of this article.

Videos S1–6: Original (odd-numbered) and distortion-corrected (even-numbered) example datasets. For each video, three rows of images are shown corresponding to hyperpolarized [1-^{13}C]pyruvate, ^{13}C-bicarbonate and [1-^{13}C]lactate respectively, and the *z* axis is shown concatenated across rows, with the head to the left. The TR for each metabolite is approximately 1.2−1.4 s, which is not depicted here.
Videos S7–8: Original 7 and distortion-corrected 8 single-slice data overlaid on an anatomical proton reference. Columns refer to pyruvate, bicarbonate and lactate images respectively. The colour axis is scaled relative to the maximum intensity in the image with values < 0.2 set to transparent.